Validation of registration techniques applied to XRD signals for stress evaluations in titanium alloys

Benoit Voillot, Jean Lou Lebrun, René Billardon, François Hild

▶ **To cite this version:**

Benoit Voillot, Jean Lou Lebrun, René Billardon, François Hild. Validation of registration techniques applied to XRD signals for stress evaluations in titanium alloys. Experimental Mechanics, 2018, 58 (8), pp.1265-1280. 10.1007/s11340-018-0391-6 . hal-01744738

HAL Id: hal-01744738
https://hal.science/hal-01744738

Submitted on 27 Mar 2018

HAL is a multi-disciplinary open access archive for the deposit and dissemination of scientific research documents, whether they are published or not. The documents may come from teaching and research institutions in France or abroad, or from public or private research centers.

L'archive ouverte pluridisciplinaire **HAL**, est destinée au dépôt et à la diffusion de documents scientifiques de niveau recherche, publiés ou non, émanant des établissements d'enseignement et de recherche français ou étrangers, des laboratoires publics ou privés.

Experimental Mechanics manuscript No.
(will be inserted by the editor)

Validation of registration techniques applied to XRD signals for stress evaluations in titanium alloys

Benoit Voillot · Jean-Lou Lebrun · René Billardon · François Hild

Received: date / Accepted: date

Abstract To estimate stresses near specimen surfaces, X-ray diffraction (XRD) is applied to titanium alloys. Some of these alloys are difficult to study since they are composed of various phases of different proportions, shapes and scales. For millimetric probed volumes, such multi-phase microstructures induce shallow and noisy diffraction signals. Two peak registration techniques are introduced and validated thanks to tensile tests performed on two titanium alloy samples.

Keywords DIC · in-situ test · integrated methods · stress analyses · XRD

1 Introduction

High performance titanium alloys are used in aeronautical industries and especially large forgings (*e.g.,* landing gears). These critical parts of an aircraft are submitted to various heat and mechanical treatments [1]. One of the consequences are changes in microstructure, roughness and residual

B. Voillot, R. Billardon
Safran Landing Systems, Inovel Parc Sud
7 rue Général Valérie André, 78140 Vélizy-Villacoublay, France
E-mail: voillot@lmt.ens-cachan.fr

B. Voillot, J.-L. Lebrun, F. Hild
LMT, ENS Paris-Saclay / CNRS / Univ. Paris-Saclay
61 avenue du Président Wilson, 94235 Cachan Cedex, France

stresses [2,3]. Each of these parameters has an impact on the global in-service mechanical behavior of the whole structure and in particular in fatigue [4–6]. It is of high interest to be able to describe the effect of these treatments by several ways (*e.g.,* microstructure studies, roughness measurements). Another way to quantify these treatments is *via* residual stress analyses. Various methods exist to estimate residual stresses. Most of them are destructive (*e.g.,* incremental hole [7], contour methods [8]). To carry out analyses on in-service structures, nondestructive methods need to be performed.

One of the most popular nondestructive stress analysis techniques is X-ray diffraction (XRD) [9–14]. Various post-processing algorithms are used to evaluate stresses from XRD measurements [15, 12]. Among them the centered barycenter is common [12–14]. It consists in determining positions of the diffraction peak by the sliding center of gravity of all the points in its neighborhood. This method is very powerful for well-defined peaks. However it is known that stress analyses are challenging for titanium alloys, especially multi-phase grades [16,17]. This difficulty comes from high levels of fluorescence and high noise to signal ratios. As a result, it is difficult to accurately locate diffraction peaks [18]. Other post-processing methods are currently used to register diffraction peaks. Peak to peak registrations are also utilized in some cases [12]. A prerequisite is good similarity between peaks, which is not necessarily very suitable for two-phase materials or materials whose fluorescence varies with the angle of measurement. The latter phenomenon is observed in two-phase titanium alloys [13,4]. All these methods are implemented in most of commercial codes (*e.g.,* Stressdiff [19] or Leptos by Bruker [20]). The last method used in existing commercial codes consists in modelling peaks with a mathematical function (*e.g.,* Lorentz, Pearson VII, pseudo-Voigt or Gauss distributions [12]). This post-processing method (*i.e.,* model with a known function) will be used to benchmark the integrated approach proposed herein.

Stress analyses are most of the time benchmarked with stress-free configurations (*i.e.,* powder of the material [12,21]) or standard coupon [16]. One of the issues with the former is finding a

powder whose lattice structure is close to those of the material of interest. In some cases such as multi-phase materials, it is hard or impossible to get powder of the real material. An alternative route is to monitor a mechanical test with XRD means. Tools used for evaluating residual (*i.e., ex-situ*) stresses can also determine applied (*i.e., in-situ*) stresses [22] during mechanical tests. Either the testing machine is put within the goniometer [23] or the goniometer is mounted inside the testing machine [24]. This methodology will be used to validate the stress estimates reported herein. Further, it will also be combined with 2D digital image correlation [25] to monitor surface displacements. Such combination has been used to validate XRD measurements and determine stress/strain curves in biaxial experiments on thin films [26,27].

To address the issue of high noise to signal ratio associated with titanium alloys, it is proposed to require the peak shifts to be expressed in terms of the quantities of interest, namely, the sought elastic strains (or stresses). When a peak registration procedure is used it corresponds to an integrated approach as used in digital image correlation [28–31], stereocorrelation [32–35] and digital volume correlation [36]. The outline of the paper is as follows. First, the studied alloys and the experimental setup are presented. Then the two registration techniques used herein are introduced. Last, the results obtained on the two titanium alloys are analyzed and validated.

2 Studied alloys

Two two-phase titanium alloys are studied herein. First, Ti64 alloy is selected for benchmark purposes because it is well-known and its microstructure is favorable for XRD measurements [16, 17]. Second, Ti5553 is a two-phase material used by Safran Landing Systems for landing gears [37]. The composition of Ti64 is given in Table 1. It is composed of 6 $wt\%$ of Aluminum and 4 $wt\%$ of Vanadium. It is a quasi pure α-phase (*i.e.,* 95 $wt\%$ of α-phase and only 5 $wt\%$ of β-phase). The α-phase is hexagonal close packed (HCP) and the β-phase is body centered cubic (BCC).

Element	Al	V	Ti
$wt\%$	6	4	Bal.

Table 1: Chemical composition of Ti64

Alloying elements of Ti5553 are mostly composed of 5 $wt\%$ of Aluminum, 5 $wt\%$ of Vanadium, 5 $wt\%$ of Molybdenum, and 3 $wt\%$ of Chromium (Table 2). It is a quasi β-metastable material. It contains 60 $wt\%$ of α-phase and 40 $wt\%$ of β-phase. Such metastable alloys are of interest for aeronautical applications thanks to their high specific strength. Only the α-phase will be considered in XRD measurements. The same lattice family (*i.e.,* {213}-planes) will be studied. The proportion of β-phase in Ti64 can be neglected. This is not the case for Ti5553 alloys for which the stress evaluation will be incomplete.

Element	Al	V	Mo	Cr	Fe	C	O	Ti
$\%wt$	5	5.2	5.2	2.7	0.4	0.009	0.154	Bal.

Table 2: Chemical composition of Ti5553

Figure 1 shows micrographs of both alloys. For Ti64 the α-grains are observed as well as the former β-grains. For Ti5553 the matrix of the primary β-phase appears in gray and contains primary and secondary α-nodules (a few μm in diameter) and lamellae (at sub-μm scale) in black [38]. The coexistence of these two phases is an issue for XRD analyses [39, 40].

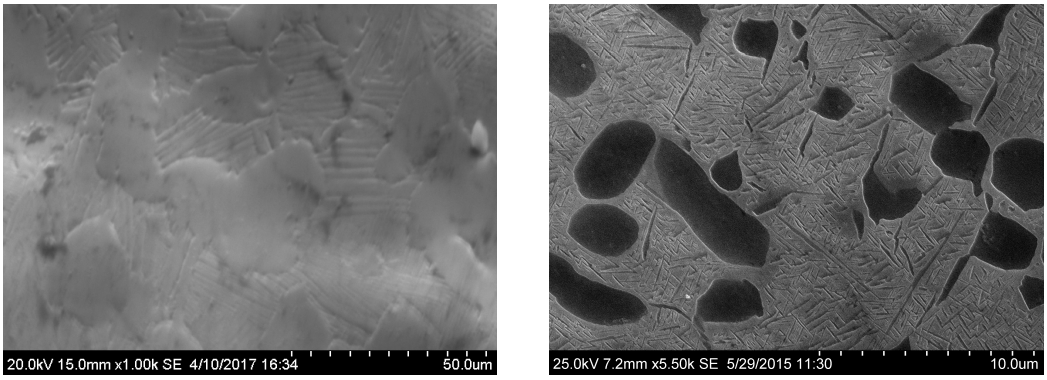

(a) (b)

Fig. 1: Micrographs of Ti64 (a) and Ti5553 (b) alloys

Figure 2 is the result of an EBSD analysis of Ti64. The area observed in Figure 2(b) is the same as the micrography of Figure 1(a). Most of the alloy is made of α-grains at micrometer scale and there is no clear orientation of grains. It results that the α-phase lattices of the probed volume is always in Bragg's conditions for Ti64 alloy.

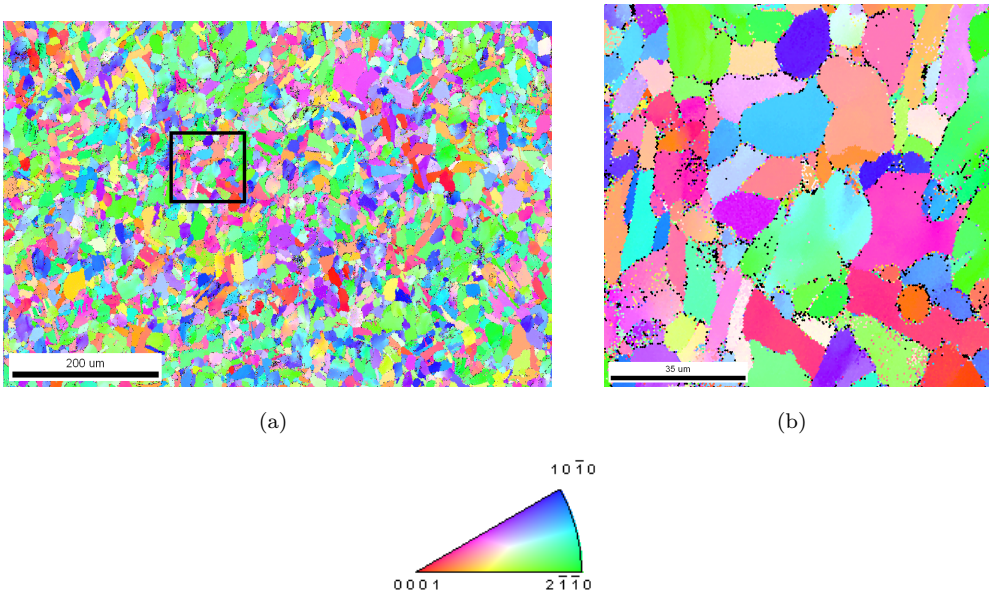

Fig. 2: (a) EBSD orientation map of Ti64 sample (α-indexation). The black box is enlarged in sub-figure (b)

Figure 3 shows that the size of β-grains is millimetric. This dimension is comparable to the extent of the volume probed by the X-ray beam (*i.e.,* 1 mm in diameter for a depth of 5 μm, see Section 3). For one XRD analysis, only few grains of the β-phase are analyzed. It results that the β-phase lattices of the probed volume are not always in Bragg's conditions. Consequently, the β-phase is not adequate for stress analyses. This EBSD picture also reveals that there is no significant texture.

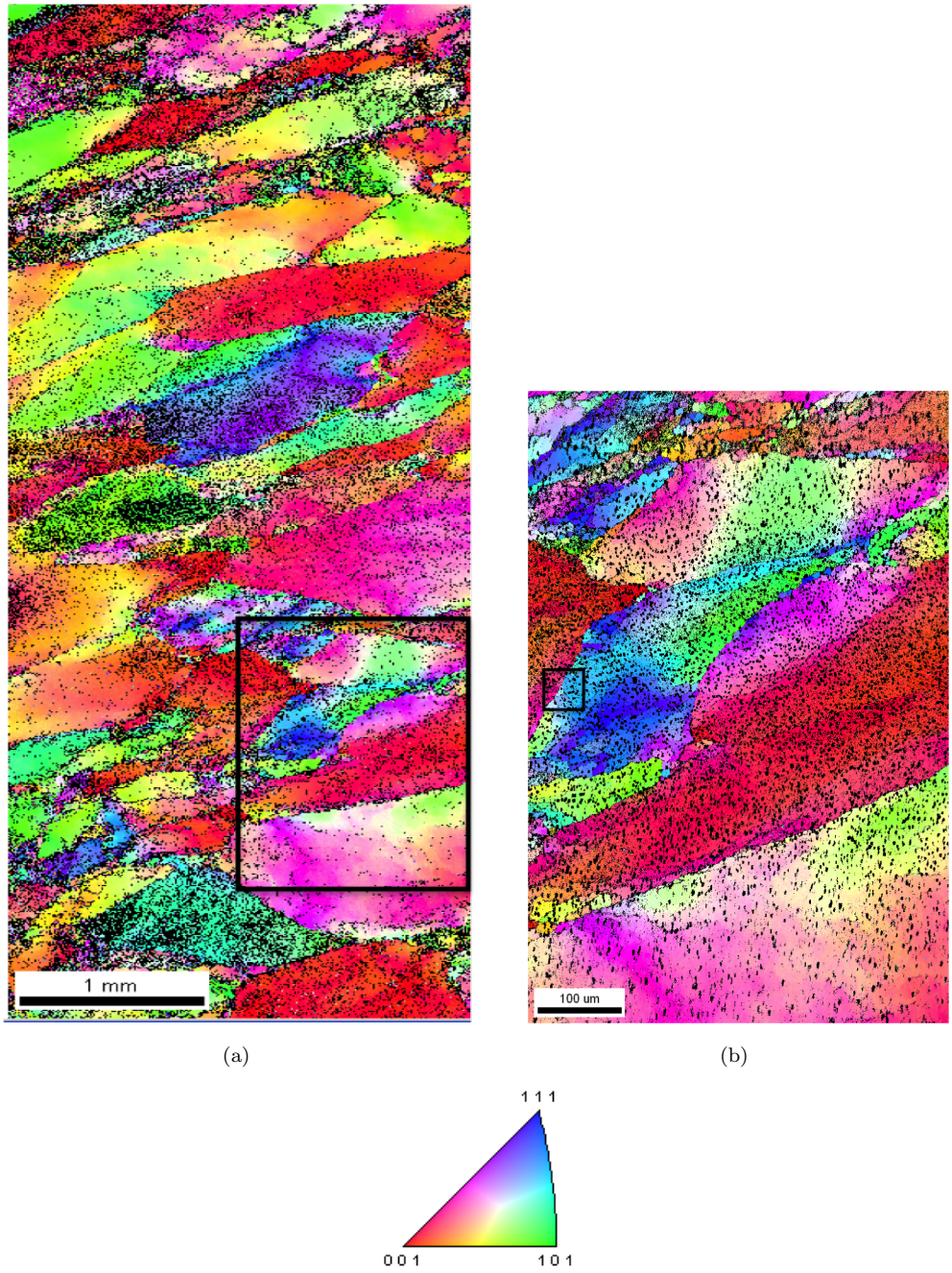

Fig. 3: (a) EBSD orientation map of Ti5553 sample (β-indexation). The black rectangle is enlarged in (b). The boxed detail is shown in Figure 4

In Figure 4, a zoom of Figure 3(b) is shown. The α- and β-phases are now distinguished. The orientations of β-grains are not linked to one another. The α-phase made of nodules and lamellae do not show any preferential orientation with the β-grain in which they are nested [41]. This is of prime importance for XRD measurements since a random orientation of α-grains in the interaction volume ensures that Bragg's condition will be satisfied for the α-phase in any probed direction. A complete stress estimation is possible with a lab goniometer [12, 14] for this phase.

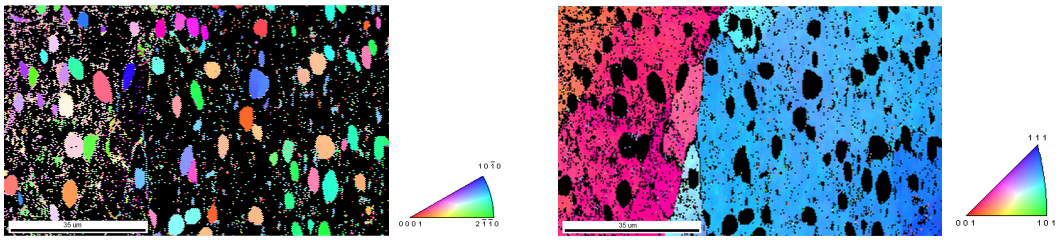

(a) α-phase (b) β-phase

Fig. 4: EBSD orientation map of Ti5553 sample (zoom of Figure 3(b)). (a) α-indexation, and (b) β-indexation

Figure 5 compares the signal to noise ratio for both alloys with the {213} family of planes of the α-phase. For the same diffraction conditions the diffraction peak is better defined in Ti64 in comparison with Ti5553. This is a direct consequence of two different microstructures (Figures 2, 3 and 4). Consequently, it is expected that the peak positions are more difficult to determine with Ti5553 than Ti64 alloys, which will presumably have an impact on stress evaluations [18, 42]. The aim of the following analyses is to assess the feasibility of XRD analyses under such challenging conditions.

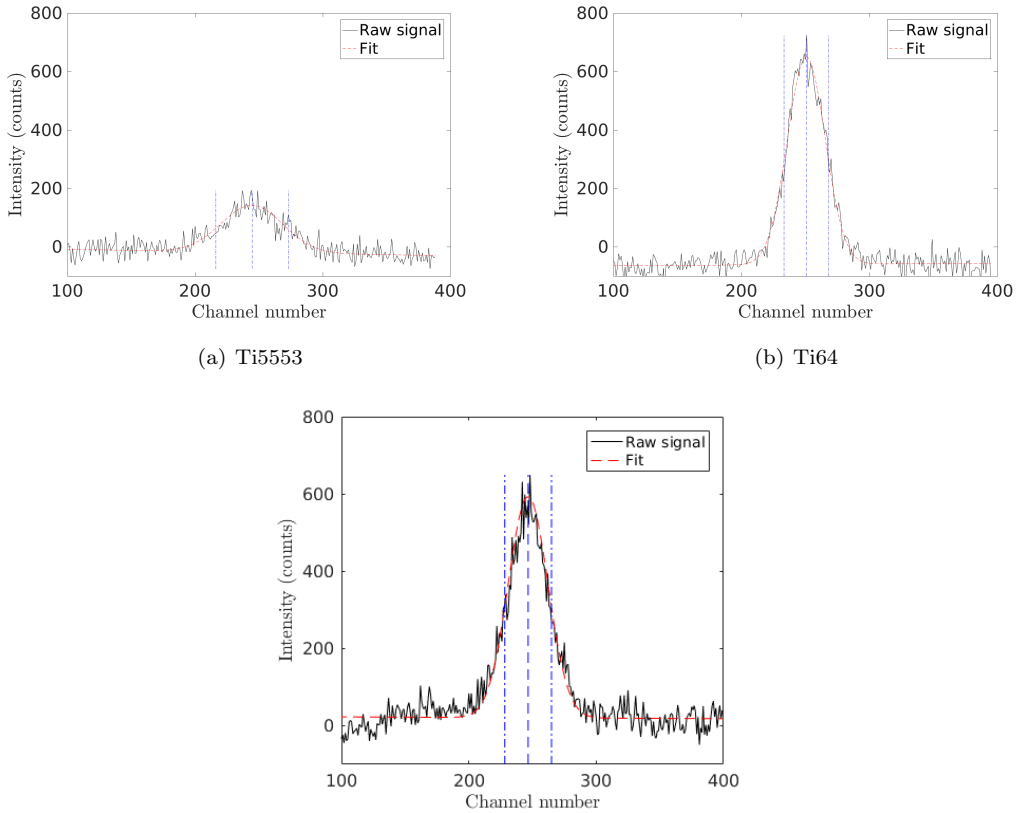

(a) Ti5553

(b) Ti64

(c) Pure titanium powder

Fig. 5: Diffractograms of the two studied alloys and of pure titanium powder (the same dynamic range is used for all plots)

3 Experimental setup

The experimental setup consists of a biaxial testing machine [43] mounted in the X-ray goniometer (Figure 6). The advantage of such testing machine, which can also be used in an SEM chamber, is that two actuators are used to load the sample. In the chosen control mode, the center of the sample is motionless. It was checked (a posteriori) with DIC analyses that the maximum motion was less than 10 μm, which is negligible with respect to the probed surface (*i.e.*, 1 mm^2). The

testing machine is moved and relocated into the goniometer at each step of loading in order to acquire images for DIC purposes.

Fig. 6: *In-situ* tensile test enabling for XRD stress analyses

The goniometer used in the present work follows the χ-method [12], see Figure 7. The radius of the goniometer is 150 mm. It is equipped with a mobile head composed of the X-Ray source (X) and a single linear position sensor (LPS) that turns about a motionless coupon to be analyzed. The LPS sensor gives a 1D measurement of diffraction intensity. S1, S2, S3 are the basis axes corresponding to the analyzed sample S. Here as the coupon is motionless during all the measurements, the basis corresponds to the goniometer reference axes. 2θ is the diffraction angle between the incident and diffracted beams. For diffraction in titanium alloys, a copper source was selected. The use of a collimator gives a probed volume of the order of 1 mm^2 $\times$ 5 μm. A Nickel (K_β) filter is added in front of the LPS sensor to only analyze the K_α rays of the copper source. The duration of X-Ray exposure (*i.e.,* 3 min per diffractogram), intensity and voltage (*i.e.,* 20 mA and 40 kV) are a compromise between duration of measurement and diffraction peak quality in the current conditions (Figure 5).

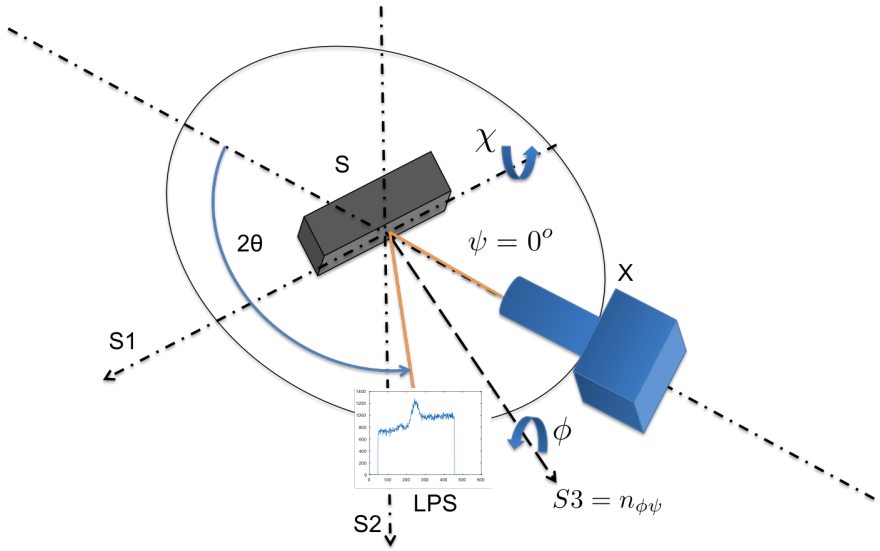

Fig. 7: Sketch of the linear position sensor (LPS), X-ray source (X), analyzed sample S in the goniometer (after Ref. [12])

To have access to various zones on the diffraction sphere, rotations are made possible in the Eulerian cradle of the goniometer as illustrated in Figure 8. Along the S3 axis (*i.e.,* normal to the sample surface and the vertical axis of the goniometer) various angles ϕ are reached. They correspond to the main direction of measurement. The rotation along the S1 axis allows various angles χ or ψ to be probed. For one single stress analysis, thirteen diffractograms at various angular positions ψ ranging from $-50°$ and $50°$ are selected [12]. It is worth noting that the goniometer does not allow for oscillations during measurements.

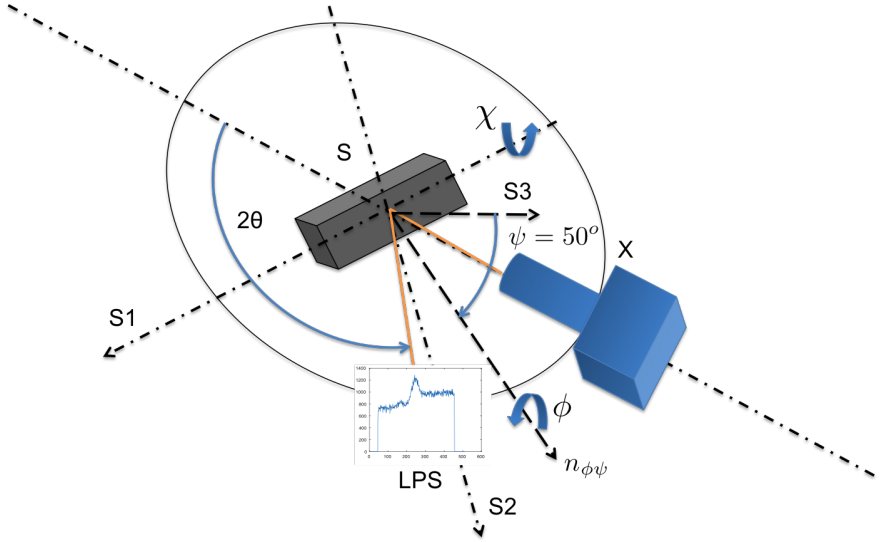

Fig. 8: Sketch of a rotation of $\psi = -50°$ around χ axis and locations reached thanks to the Eulerian cradle of χ-method goniometer (after Ref. [12])

When the moving head is turning within the goniometer, the center of the surface area of the volume probed by the X-ray beam is moving by less than 0.1 mm. This observation ensures that the same volume of material is always impacted by X-rays at each angle of measurement. To check the errors due to the use of the goniometer, an analysis on a stress-free powder made of pure titanium was carried out before and after each measurement campaign. All evaluated stress components varied about 0 MPa with a standard deviation of 10 MPa. Further, a height change of 50 μm of the coupon led to an error in stress of about 4 MPa. This stability of the beam interaction with the probed surface and the verification of stress-free evaluations with a Ti powder are indications of good working conditions for stress analyses.

In order to validate the stress analyses performed on titanium alloys, in particular the new integrated method, dog-bone samples (Figure 9) were machined. The coupon has been designed to ensure a controllable and homogenous stress and strain area in the central area of the coupon where X-ray analyses are performed. The aim is to carry out *in-situ* tensile tests. It is an alternative

way to benchmark stress analyses via XRD. Usual validations are carried out with standard coupons [16] or powders assumed to be stress-free. For pure titanium, powders exist and were proven to yield good results for the goniometer used herein [12]. However, the lattice parameters of pure titanium are slightly different for Ti5553 or Ti64 alloys. The position and quality of peaks also vary (Figure 5). Consequently, having reliable results on titanium powders does not necessarily ensure trustworthy estimates for titanium alloys. The Ti64 grade will be the reference material since it is more suitable to XRD analyses. The Ti5553 alloy will be subsequently studied once the registration procedures have been validated.

(a) (b)

Fig. 9: Coupon for *in-situ* tests. (a) Dog-bone geometry (ligament width: 6 mm, thickness: 0.5 mm, radius of the hour-glass shape: 65 mm). (b) Speckle pattern used for DIC procedures with an unpainted area to allow for XRD measurements. The area probed by the X-ray beam is depicted in orange.

In-situ uniaxial tensile tests are carried out under a load control mode. The direction ϕ is chosen to coincide with the longitudinal direction S1 of the coupon (Figures 7 and 9). To measure the total strains on the sample surface, 2D DIC will be used. The sample surface is coated with black and white paints in order to create a speckle pattern (Figure 9(b)). To avoid any bias, the analyzed XRD zone is not covered. When the targeted load level is reached, the sample and testing machine are moved out of the goniometer to acquire pictures. A telecentric lens is mounted on the digital camera to minimize as much as possible the spurious effects associated with out of plane motions. The actuators of the testing machine induce stress variations less than 16 MPa (standard

deviation) for the investigated stress range. An isostatic set-up ensures the testing machine to be positioned very precisely in the goniometer. The angular standard uncertainty in relocation is less than 2°, which corresponds to a small error in final stress estimations. The spatial repositioning error is less than 0.1 mm, a value ten times smaller than the probed surface diameter.

4 Stress extraction

When a material is loaded or has residual stresses, crystal lattices deform. XRD procedures measure the variations of inter-reticular distances by analyzing diffraction peaks in (poly)crystalline materials [14, 21, 13, 39]. In the case of titanium alloys analyzed by a copper source, the peak commonly used to carry out stress analyses diffracts at an angle $\approx 140°$ [10] and corresponds to the $\{213\}$ family of the α-phase, which can be found in both Ti64 and Ti5553 alloys [16, 37, 3]. The inter-reticular distance for this angle is given by the dimension of the HCP crystal structure where the edges of the hexagon are $a = 0.295$ nm and the height of the lattice is $c = 0.468$ nm [44]. The link between diffraction peak angle and inter-reticular distances is given by Bragg's law

$$2d^{\{213\}} \sin\theta = \lambda_{K\alpha Cu} \tag{1}$$

where $d^{\{213\}}$ is the inter-reticular distance for $\{213\}$ planes of the α-phase, θ the diffraction angle, and $\lambda_{K\alpha Cu}$ the wavelength of the X-ray beam (*e.g.,* copper source with $\lambda_{K\alpha Cu} = 0.154$ nm). Peak registrations presented in the following do not dissociate $K_{\alpha 1}$ and $K_{\alpha 2}$ rays. Elastic stresses near the sample surface in α-phases are evaluated via XRD by estimating peak shifts [12, 14].

4.1 From channels to stresses

Figure 10 describes the whole procedure used from the acquisition of diffractograms by the goniometer equipped with a linear position sensor (LPS) that gives an information expressed in channels x to stress estimations.

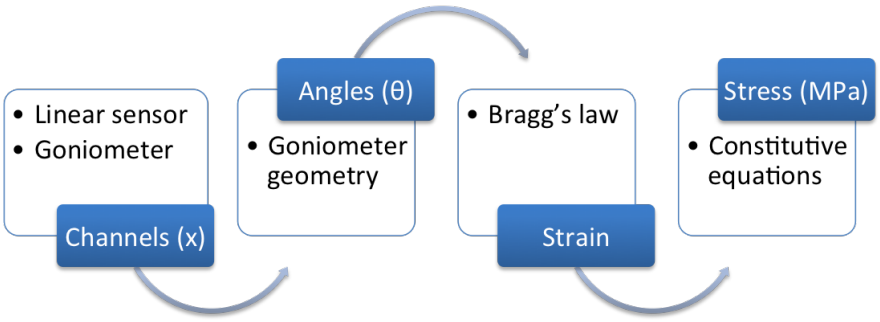

Fig. 10: General procedure used in stress analyses

The first step consists in transforming the information expressed in channels into angular positions 2θ. The sensor used herein is discretized into 512 channels. The raw signal is collected in terms of counts of X-Ray intensity received per channel. The relationship between channel x and angular position depends on the geometry of the goniometer (Figure 11)

$$2\theta(x) = 2\theta_{ref} + \tan^{-1}\left(\frac{\ell}{L}\frac{x - x_{ref}}{x_{max}}\right) \tag{2}$$

with

$$x_{ref} = \frac{x_{max} + 1}{2} \tag{3}$$

where $2\theta_{ref}$ is the angle corresponding to the central channel of the linear sensor (this angle is equal to 140° thanks to the use of Ti powder). The ratio ℓ/L is a geometric parameter of the goniometer (*i.e.,* it depends on the length of the LPS sensor, $\ell = 50$ mm, and the distance between the analyzed surface and the sensor, $L = 150$ mm). The angles ϕ and ψ determine the location of the goniometer during one single measurement with ϕ the main measurement direction and ψ the incidence angle of the X-ray source and sensor (see Figures 7 and 8).

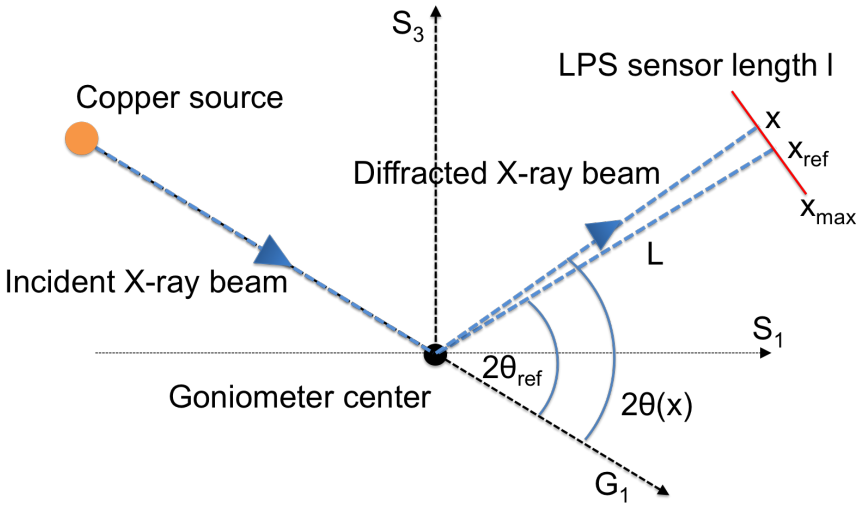

Fig. 11: Linear position sensor (LPS) and goniometer geometry

One key element of XRD analyses is the extraction of the angular position $\theta_{\phi\psi}$ of the diffraction peak. It will be discussed in the next section. Once this information is available, the next step consists in expressing the lattice strain $\epsilon_{\phi\psi}$ as a function of the angular position of the diffraction peak

$$\epsilon_{\phi\psi} = \ln\left(\frac{d_{\phi\psi}^{\{213\}}}{d_0^{\{213\}}}\right) = -\ln\left(\frac{\sin\theta_{\phi\psi}}{\sin\theta_0}\right) \tag{4}$$

where $d_{\phi\psi}^{\{213\}}$ denotes the inter-reticular distance for the deformed configuration, $d_0^{\{213\}}$ the inter-reticular distance for the undeformed configuration, and $2\theta_0$ the corresponding diffraction angle. To get an estimate of the stress tensor in one direction, several measurements (*i.e.,* angular positions ψ) are needed for each point of analysis [12]. Inter-reticular distances $d_{\phi\psi}$ and corresponding angles $\theta_{\phi\psi}$ depend on the main measurement direction ϕ but also on the incidence angle of the X-ray source ψ. As measurements are carried out very close to the sample surface, the normal stress component perpendicular to the surface (along the axis S3, see Figure 7) will be assumed to vanish ($\sigma_{33} = 0$), in order to be consistent with a traction-free surface. The relationship between

stress and elastic strain components is then given by

$$\tilde{\epsilon}_{\phi\psi} = -\frac{1}{2}S_2^{\{213\}}\sigma_\phi \sin^2\psi - \frac{1}{2}S_2^{\{213\}}\tau_\phi \sin 2\psi + \tilde{\epsilon}_{\psi=0} \tag{5}$$

where $\tilde{\epsilon}_{\phi\psi} = \ln(\sin\theta_{\phi\psi})$, $S_1^{\{213\}}$ and $S_2^{\{213\}}$ are the X-Ray elasticity constants depending on the diffracting planes, and $\tilde{\epsilon}_{\psi=0} = \ln(\sin\theta_0) - S_1^{\{213\}}\mathrm{tr}(\boldsymbol{\sigma})$ will be referred to as composite strain. The normal and shear stresses are denoted by $\sigma_\phi \equiv \sigma_{\phi\phi}$ and $\tau_\phi \equiv \sigma_{\phi 3}$, respectively. In the present case elastic isotropy and homogeneity are assumed since anisotropy in $\{213\}$ planes of α lattice is relatively small, so that $S_1^{\{213\}}$ and $S_2^{\{213\}}$ are invariant for any probed angle for the α-phase. It is worth noting that with the present setting, the knowledge of θ_0 is not needed when using $\tilde{\epsilon}_{\phi\psi}$ instead of $\epsilon_{\phi\psi}$. However, to probe the consistency of the results, it will be checked *a posteriori* when analyzing tensile tests (in particular, the value of θ_0).

In the present case, the X-Ray elasticity parameters $S_1 = -\dfrac{\nu_\alpha}{E_\alpha}$ and $\dfrac{1}{2}S_2 = \dfrac{1+\nu_\alpha}{E_\alpha}$ depend on the Poisson's ratio ν_α and Young's modulus E_α of the α-phase (*i.e.,* $\dfrac{1}{2}S_2 = 11.9 \times 10^{-6}$ MPa^{-1} and $S_1 = -2.64 \times 10^{-6}$ MPa^{-1} [45,46]. These values correspond to $E_\alpha = 109$ GPa and $\nu_\alpha = 0.3$. The stress tensor components σ_ϕ and τ_ϕ are determined by least squares minimization

$$\min_{\sigma_\phi,\tau_\phi,\tilde{\epsilon}_{\psi=0}} \sum_\psi [\tilde{\epsilon}_{\phi\psi} + \frac{1}{2}S_2\sigma_\phi \sin^2\psi + \frac{1}{2}S_2\tau_\phi \sin 2\psi - \tilde{\epsilon}_{\psi=0}]^2 \tag{6}$$

in addition to the composite strain $\tilde{\epsilon}_{\psi=0}$.

4.2 Registration of diffraction peaks

The previous section has shown that the sought stresses can be related to the strains (Equation (5)) or equivalently to the channel position of the diffraction peak (Equations (2)-(4)). In both cases, the location of the peaks $\theta_{\phi\psi}$ has to be determined. One of the standard approaches consists in registering the measured diffractogram with an *a priori* chosen function $0 \leq g(x) \leq 1$ whose maximum location is known (*i.e.,* $g(x = x_0) = 1$). The registration procedure consists in finding

the location x_0 of the peak in addition to other parameters needed to model the measured signal to minimize the sum of squared differences

$$\min_{x_0(\psi),\xi_0,\Delta I,I_b,D} \sum_x \eta^2(x; x_0(\psi), \xi_0, \Delta I, I_b, D) \tag{7}$$

with

$$\eta(x; x_0(\psi), \xi_0, \Delta I, I_b, D) = \frac{f(x;\psi) - I_b - Dx}{\Delta I} - g\left(\frac{x - x_0(\psi)}{\xi_0}\right) \tag{8}$$

where f is raw signal measured by XRD for the angular position ψ, x the channel position on the LPS sensor, ξ_0 the width of the function that is proportional to the full width at half maximum (FWHM), and $\Delta I = I_{\max} - \langle I_{bgl} \rangle$ the peak intensity above the background line (bgl). In the present case, the background intensity is modelled with a linear function $I_{bgl}(x) = I_b + Dx$. Consequently, there are five unknowns to be determined, namely, x_0, ξ_0 and $I_{\max}$ that characterize the diffraction peak, in addition to I_b and D that describe the background line (Figure 12).

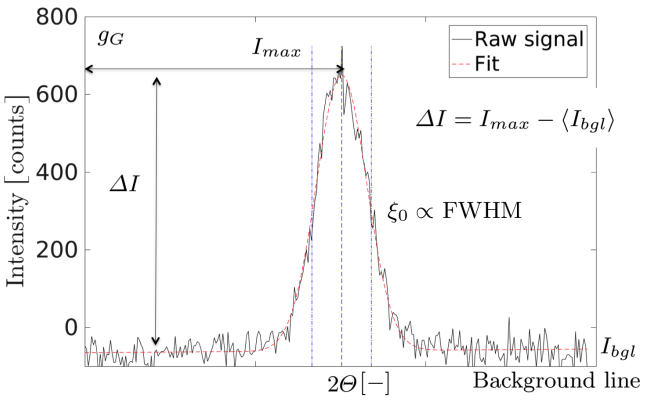

Fig. 12: Peak model and notations

Each diffractogram is analyzed independently (*i.e.,* for each considered angle ψ) with a registration technique that can be referred to as diffraction signal correlation or DSC (*i.e.,* it is the one dimensional version of (2D) digital image correlation or (3D) digital volume correlation [25,

47]. A Gauss-Newton algorithm is implemented to minimize the sum of squared differences (7) for each considered angle ψ. The covariance matrix associated with the evaluated parameters, which are gathered in the column vector $\{\mathbf{p}\} = \{x_0, \xi_0, \Delta I, I_b, D\}^\dagger$, reads [47]

$$[\mathbf{Cov_p}] = \frac{\gamma^2}{\Delta I^2}[\mathbf{M}]^{-\mathbf{1}} \tag{9}$$

where γ is the standard deviation of the acquisition noise that is assumed to white and Gaussian, and $[\mathbf{M}]$ the Hessian used in the minimization scheme

$$[\mathbf{M}] = [\mathbf{m}]^\dagger[\mathbf{m}] \tag{10}$$

with

$$[\boldsymbol{m}] = \begin{bmatrix} \frac{\partial \eta}{\partial x_0}(x) & \frac{\partial \eta}{\partial \xi_0}(x) & \frac{\partial \eta}{\partial \Delta I}(x) & \frac{\partial \eta}{\partial I_b}(x) & \frac{\partial \eta}{\partial D}(x) \\ \vdots & \vdots & \vdots & \vdots & \vdots \end{bmatrix} \tag{11}$$

This covariance matrix allows the resolution [1] of the registration technique to be assessed [47]. The standard resolution of the peak position is then equal to the diagonal term of $[\mathbf{Cov_p}]$ corresponding to x_0, provided the other parameters do not change.

The influence of the peak position uncertainty on stress resolutions is easily computed since the stress extraction is a linear least squares problem in terms of $\tilde{\epsilon}_{\phi\psi}$ (see Equation (6)). The covariance matrix of the stress extraction technique reads

$$[\mathbf{Cov}_\sigma] = [\mathbf{C}]^{-\mathbf{1}}[\mathbf{c}]^\dagger[\mathbf{Cov}_\epsilon][\mathbf{c}][\mathbf{C}]^{-\mathbf{1}} \tag{12}$$

with

$$[\mathbf{C}] = [\mathbf{c}]^\dagger[\mathbf{c}] \tag{13}$$

and

$$[\mathbf{c}] = \begin{bmatrix} \frac{1}{2}S_2 \sin^2\psi & \frac{1}{2}S_2 \sin 2\psi & 1 \\ \vdots & \vdots & \vdots \end{bmatrix} \tag{14}$$

[1] The resolution of a measuring system is the "smallest change in a quantity being measured that causes a perceptible change in the corresponding indication" [48].

Commercial softwares (*e.g.,* Stressdiff [19] or Leptos [20]) use peak positions issued from such minimization to end up with so-called $\sin^2\psi$ methods [12,13,4]. This procedure will serve as benchmark for the validation of the following integrated procedure.

Given the fact that the peak positions are parameterized in terms of the sought stresses and composite strain (*i.e.,* $x_0 = x_0(\sigma_\phi, \tau_\phi, \tilde{\epsilon}_{\psi=0})$, see Equations (2) and (4)), the previous minimization can be performed over the *whole* set of diffractograms

$$\min_{\sigma_\phi,\tau_\phi,\tilde{\epsilon}_{\psi=0},\xi_0,\Delta_I,I_b,D} \sum_{\psi}\sum_{x} \eta_I^2(x,\psi;\sigma_\phi,\tau_\phi,\tilde{\epsilon}_{\psi=0},\xi_0,\Delta_I,I_b,D) \tag{15}$$

with

$$\eta_I(x,\psi;\sigma_\phi,\tau_\phi,\tilde{\epsilon}_{\psi=0},\xi_0,\Delta_I,I_b,D) = \frac{f(x,\psi)-I_b-Dx}{\Delta I} - g\left(\frac{x-x_0(\sigma_\phi,\tau_\phi,\tilde{\epsilon}_{\psi=0})}{\xi_0}\right) \tag{16}$$

This approach corresponds to integrated DSC for which the sought quantities are directly determined from the registration procedure and do not need an additional minimization step. A Gauss-Newton scheme is also implemented and the initial guess of the sought parameters comes from a first non integrated analysis. The covariance matrix associated with the evaluated parameters, which are gathered in the column vector $\{\mathbf{p_I}\} = \{\sigma_\phi, \tau_\phi, \tilde{\epsilon}_{\psi=0}, \xi_0, \Delta_I, I_b, D\}^\dagger$, reads

$$[\mathbf{Cov_{p_I}}] = \frac{\gamma^2}{\Delta I^2}[\mathbf{M_I}]^{-\mathbf{1}} \tag{17}$$

where $[\mathbf{M_I}]$ is the approximate Hessian used in the global minimization scheme

$$[\mathbf{M_I}] = [\mathbf{m_I}]^\dagger[\mathbf{m_I}] \tag{18}$$

with

$$[\boldsymbol{m}_I] = \begin{bmatrix} \frac{\partial\eta_I}{\partial\sigma_\phi}(x,\psi) & \frac{\partial\eta_I}{\partial\tau_\phi}(x,\psi) & \frac{\partial\eta_I}{\partial\tilde{\epsilon}_{\psi=0}}(x,\psi) & \frac{\partial\eta_I}{\partial\xi_0}(x,\psi) & \frac{\partial\eta_I}{\partial\Delta I}(x,\psi) & \frac{\partial\eta_I}{\partial I_b}(x,\psi) & \frac{\partial\eta_I}{\partial D}(x,\psi) \\ \vdots & \vdots & \vdots & \vdots & \vdots & \vdots & \vdots \end{bmatrix} \tag{19}$$

Tests have been made by selecting various distributions (*i.e.,* Gauss, Pearson VII, Lorentz). They give the same types of results without any significant improvement for any of them in terms

of registration residuals. In the following, a Gaussian distribution was selected

$$g \equiv g_G(x) = exp\left[-\left(\frac{x - x_0}{\xi_0}\right)^2\right] \tag{20}$$

A preliminary step is performed to calibrate the LPS sensor in terms of local offset corrections. The offset of the detector is determined by measuring the intensity during diffraction on a material that does not diffract at an angle close to that of {213} planes of the α-phase. Amorphous glass was chosen. The diffractogram on glass is obtained by a measurement lasting at least half an hour in order to get enough signal. After rescaling the offset is subtracted to each diffractogram used in stress analyses. Figure 13 shows that most of the spacial variations are erased and that the diffraction peak appears more clearly.

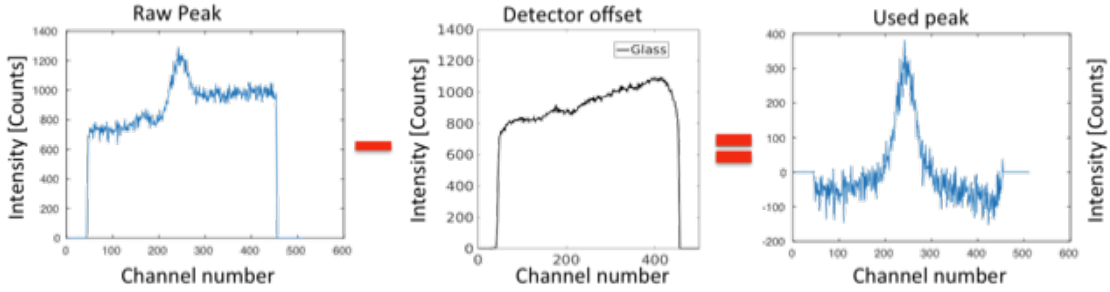

Fig. 13: Subtraction of detector offset

For the sake of convenience, the residuals that will be reported hereafter will refer to the raw acquisitions, namely,

$$\rho(x;\psi) = f(x;\psi) - \left[\Delta I g\left(\frac{x - x_0(\psi)}{\xi_0}\right) + I_b + Dx\right] \tag{21}$$

and are therefore expressed in counts. Any deviation from random noise will be an indication of model error (*i.e.,* associated with the choice of g, and elasticity). The final outputs of the two registration algorithms are σ_ϕ, τ_ϕ, and $\tilde{\epsilon}_{\psi=0} = \ln(\sin\theta_0) - S_1\mathrm{tr}(\boldsymbol{\sigma})$.

5 Results of stress analyses

5.1 Validation of the registration techniques

Six loading steps were applied (Figure 14) on the Ti64 sample ranging from 0 to 660 MPa. For such type of alloy, the maximum stress level is lower than the yield stress $\approx$ 900 MPa [4,41]. The applied stress corresponds to the applied load divided by the cross-sectional area of the sample ligament.

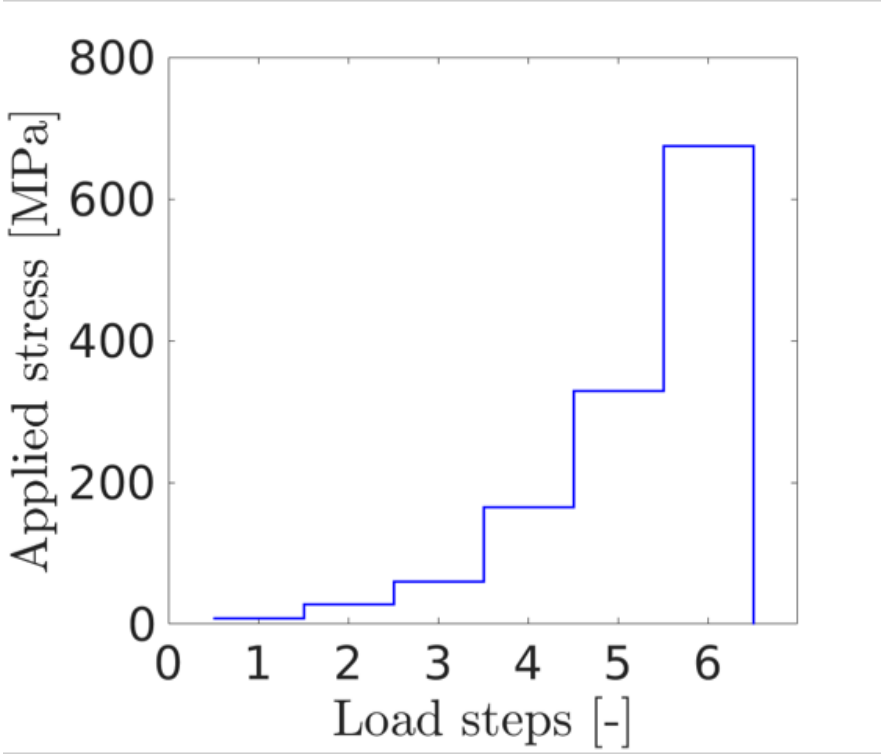

Fig. 14: Loading history during the *in-situ* tensile test on Ti64 alloy. The standard stress uncertainty is equal to 16 MPa

Figure 15 shows the root mean square registration residuals after convergence for the two DSC techniques. The overall level is virtually constant for the DSC approach (*i.e.,* 35 counts).

Interestingly, the integrated DSC residuals (*i.e.,* 39 counts), which are expected to be higher since less degrees of freedom are available, remain close to the non integrated approach. The similarity of residual levels between integrated and non integrated approaches validates the assumption of elasticity in the probed volume. These two results also show that the registration was successful via DSC and integrated DSC.

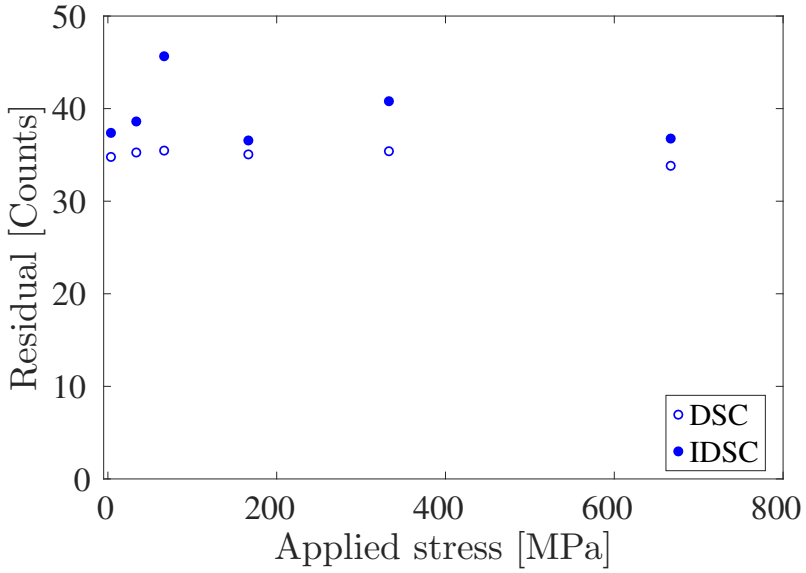

Fig. 15: Root mean square residual for Ti64 alloy for the two DSC analyses

Stress analyses can also be performed via integrated DIC [30]. The displacement field is first measured with FE-based DIC in which the kinematic field is parameterized with nodal displacements associated with an unstructured mesh (see Figure 16) made of three-noded triangles (with linear interpolation of the shape functions). Even though the central part of the sample was not speckled, the DIC code could converge (*i.e.,* helped by the convergence in the speckled area) and yields results within the XRD measured area. From these measurements, only those corresponding to the two extreme transverse rows of elements are considered and they are prescribed

as Dirichlet boundary conditions to an elastic FE analysis under plane stress hypothesis, which allows the stress field to be evaluated everywhere. Macroscopic elasticity constants used are the Young's modulus which is equal to 109 GPa and the Poisson ratio which is equal to 0.3. Figure 16 shows the longitudinal stress field for each loading step. In all the zone probed by XRD, the stress is virtually uniform and the corresponding standard deviation is less than 10 MPa for the highest load level. From this analysis, the mean longitudinal stress is reported and will be compared to the other stress evaluations.

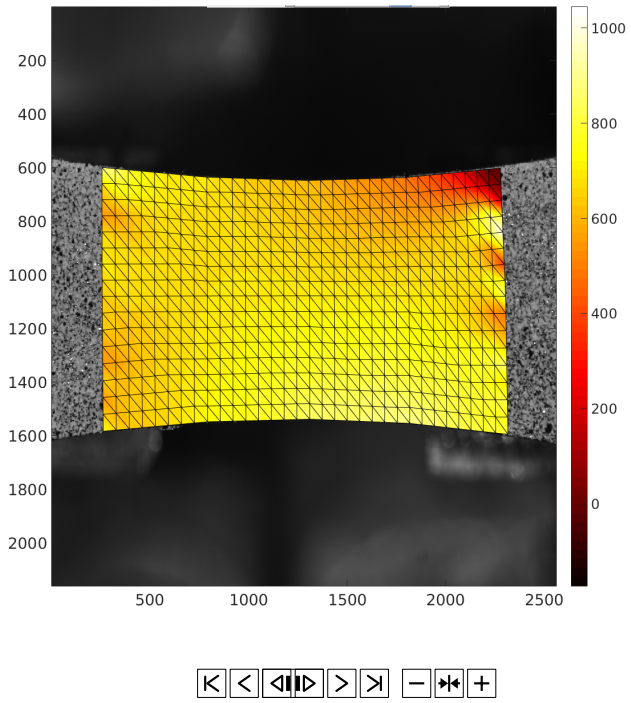

Fig. 16: Longitudinal stress (expressed in MPa) field evaluated via integrated DIC at the last loading step. Online version: history of the six analyzed steps (Figure 14)

In Figure 17, the comparison between various stress analyses is shown. In the present plot, the reference (*i.e.,* horizontal axis) is the applied stress. Integrated DIC and DIC give the same stress estimation and correspond to the mean longitudinal stress averaged over the XRD zone.

These levels are very close to the applied stress. For DIC, the measured strains are assumed to be elastic and the corresponding stresses are evaluated, as would be performed by XRD analyses (*i.e.,* without any equilibrium requirement), by using isotropic elasticity under plane stress assumption). The two DSC approaches yield results that are in very good agreement with each other and with the evaluations based on integrated DIC and load measurements.

Interestingly, the stress estimations based on both DIC results for which the strains are averaged over the zone of interest of XRD analyses are consistent with each other. This observation proves that the assumption of linear elasticity is satisfied. The fact that DSC results are consistent with IDSC, integrated DIC evaluations *and* applied stress estimates also validates the choice of X-Ray elasticity constants for the XRD measurements in Ti64 alloy.

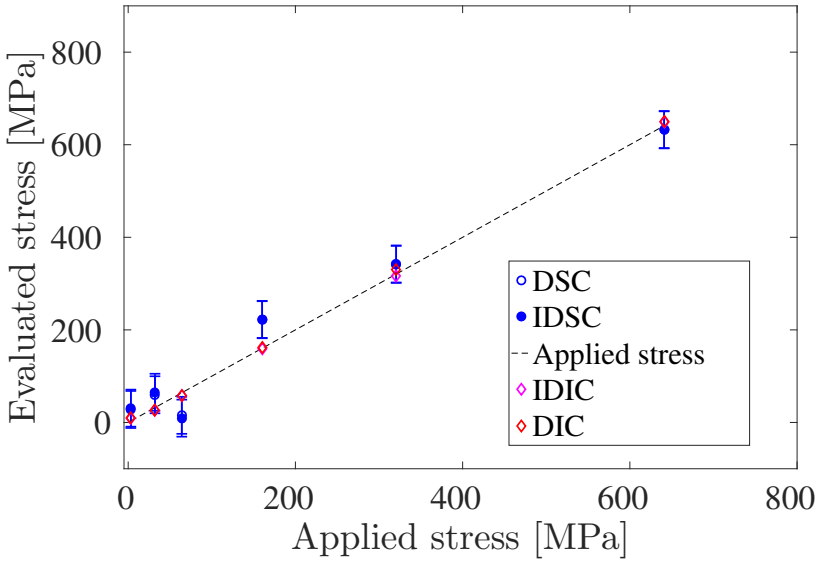

Fig. 17: Longitudinal stress σ_ϕ in Ti64 alloy coupon measured with four different evaluation techniques. The error bars depict the root mean square difference between DSC or IDSC estimates and the applied stress. The standard applied stress uncertainty is equal to 16 MPa

Figure 18 shows the error quantifications for DSC and integrated DSC with respect to the applied stress. The stress resolutions of both DSC methods are also shown. They are based on the effect of acquisition noise only (see Equations (12) and (12)). The standard resolution of the two DSC techniques is very low and of the order of 3 MPa (*i.e.,* 2.7 MPa for integrated DSC and 3.3 MPa for regular DSC). Thanks to integration, the standard resolution is decreased by 20 %. The root mean square error between the applied stress and DSC or IDSC is respectively equal to 37 MPa and 41 MPa. This level corresponds to an upper bound given the fact that load fluctuations occur (*i.e.,* inducing stress variations of the order of 16 MPa in the present case).

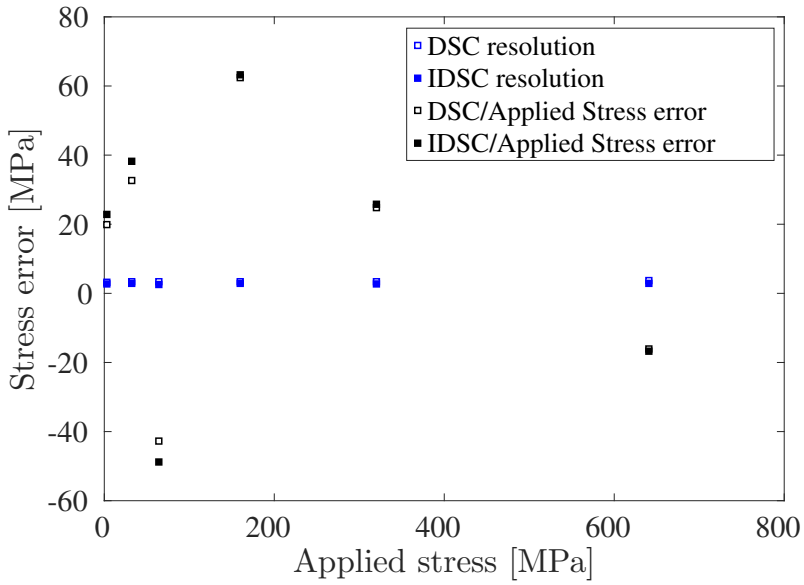

Fig. 18: Stress resolutions and errors for Ti64 alloy coupon. The standard applied stress uncertainty is equal to 16 MPa

Figure 19 shows the second output from DSC and IDSC, namely the shear stress τ_ϕ, which is expected to vanish in the present case. This result is found on average with a root mean square

error of 7 MPa for DSC and IDSC. These levels are lower than those observed for the longitudinal stress component.

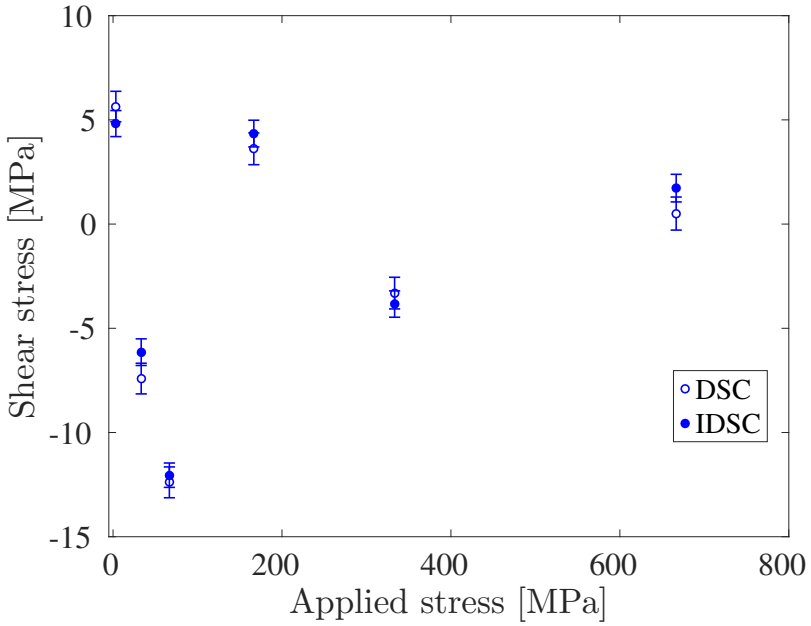

Fig. 19: Shear stress τ_ϕ in Ti64 alloy coupon estimated with DSC and IDSC. The error bars depict the root mean square difference between DSC or IDSC estimates and a vanishing shear stress. The standard applied stress uncertainty is equal to 16 MPa

The last output of the DSC codes is the composite strain $\tilde{\epsilon}_{\psi=0} = \ln(\sin\theta_0) - S_1 tr(\boldsymbol{\sigma})$. Given the fact that the trace of the stress tensor is equal to the longitudinal stress in a uniaxial tensile test, it is possible to evaluate $2\theta_0$, which is the diffraction angle for zero stress of {213} planes for the α-phase. The mean value is $2\theta_0 = 140.16^\circ$, which is close to the expected value for pure titanium (*i.e.,* 140°), see Figure 20. The corresponding standard deviation is equal to 0.019° for DSC and 0.018° for IDSC, which is 5 % lower than DSC. With Bragg's law, it is concluded that this angular uncertainty divided by $\tan(\theta_0)$ is an estimate of the longitudinal strain uncertainty

(*i.e.*, $\approx 1.2 \times 10^{-4}$ for both methods), and a longitudinal stress uncertainty of ≈ 13 MPa. This level is of the same order as the stress fluctuations induced by the tensile stage.

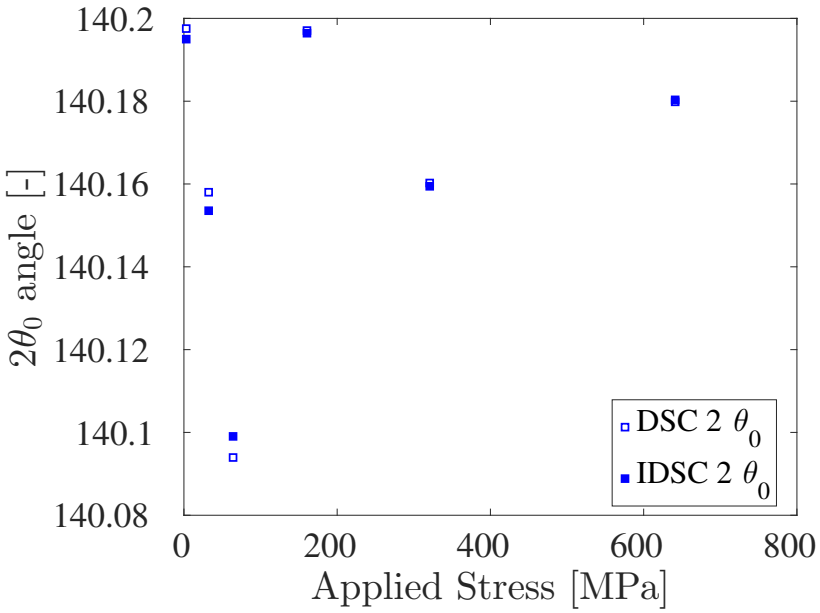

Fig. 20: Estimation of $2\theta_0$ for Ti64 alloy from the analysis of the composite strain ϵ_0. The standard applied stress uncertainty is equal to 16 MPa

Thanks to the reported consistencies of stress estimations both DSC and IDSC algorithms are now considered as validated and will be used to study the Ti5553 grade.

5.2 Application to Ti5553 alloy

For the specimen made of Ti5553 alloy, 9 loading steps and one globally unloaded step were applied and analyzed via DIC and DSC (Figure 21). The lowest stress level is 0 MPa, and the highest is 1100 MPa (the yield stress for this alloy is of the order of 1250 MPa [49]). However during electropolishing, the geometry of the sample was roughened and the thickness of the coupon has been reduced from 0.5 mm to 0.45 mm and some imperfections on the edges were created. As a

result, plasticity may occur during the test especially at high load levels. Further, the estimation of the applied stress is more delicate and thus will not be reported. The so-called DIC stresses are preferred.

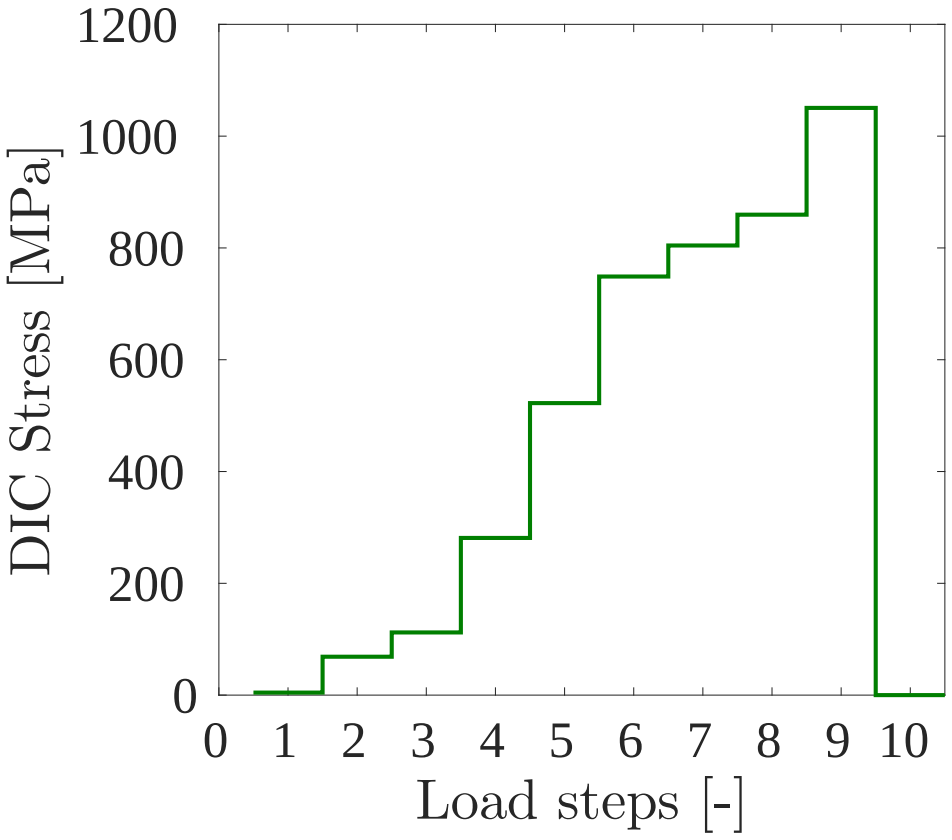

Fig. 21: Loading history during the *in-situ* tensile test on Ti5553 alloy. The standard DIC stress uncertainty is equal to 30 MPa

The occurrence of plasticity is confirmed in Figure 22 in which the stresses are evaluated with the DIC strain fields, which are assumed to be elastic. For high load levels, very high (and non physical) stress levels are observed in one area of the sample, which was not probed via XRD. It is worth noting that the last step corresponds to total unloading, which does not result in

vanishing strains and stresses, thereby confirming the presence of plastic strains in the lower part of the coupon. However, as will be illustrated in Figure 25, in the area impacted by X-rays it is believed the local stress state remains elastic and homogeneous during the whole experiment. The standard stress uncertainty corresponding to the probed area is less than 30 MPa via DIC estimations.

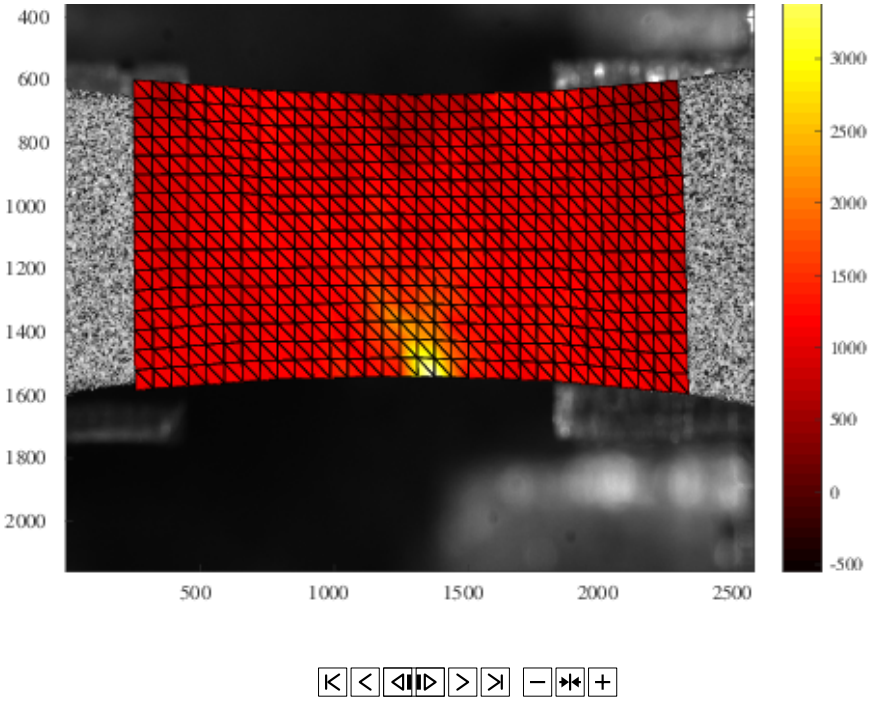

Fig. 22: Longitudinal stress (expressed in MPa) field evaluated via DIC (assuming elasticity) at the last loading step (Figure 21). Online version: history of the ten analyzed steps

Figure 23 shows root mean square residuals for both DSC approached. In the present case, the two residuals are virtually coincident for all investigated stress levels. This remarkable agreement between the two DSC techniques enables the hypothesis of elasticity to be fully validated in the present case. This observation is consistent with the fact that the α-phase is finely distributed within the probed volume (*i.e.,* of the order of 1 mm^2 $\times$ 5 μm, see Figure 2). When compared

to Ti64, the mean residuals of DSC and IDSC are lower (*e.g.,* 25 counts instead of 39 counts for IDSC in Ti64). However, the signal levels were also significantly lower (Figure 5).

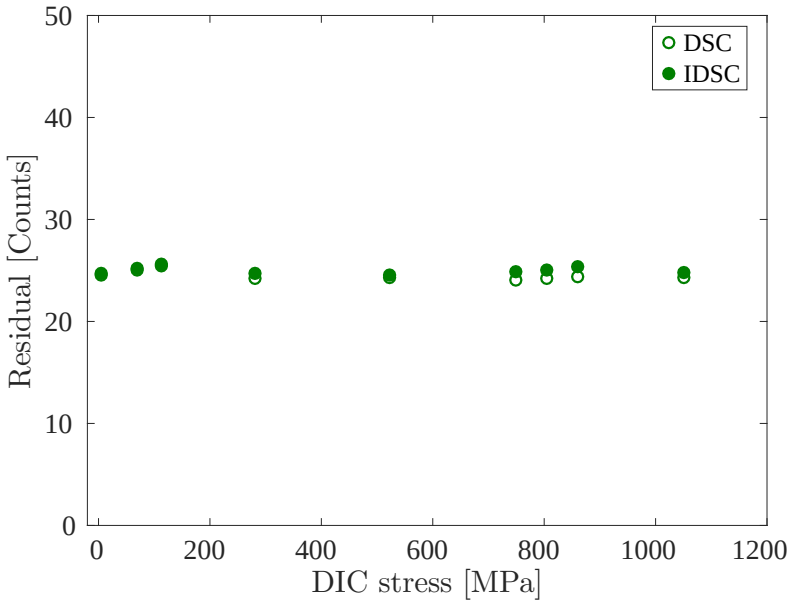

Fig. 23: Root mean square residual for Ti5553 alloy for the two DSC analyses. The standard DIC stress uncertainty is equal to 30 MPa

Due to the coexistence of two phases in the studied alloy (Figures 3 and 4), the results will first focus on elastic strains. Figure 24 displays the estimations of elastic strain by various techniques, namely integrated DIC in addition to DSC and integrated DSC. In the present case, the abscissa corresponds to the mean longitudinal strain in the XRD zone measured by DIC. The fact that DIC and integrated DIC results coincide proves that the hypothesis of elasticity was fulfilled during all the experiment and that plasticity was confined in an area that has not impacted the zone probed by XRD (as expected from Figure 22).

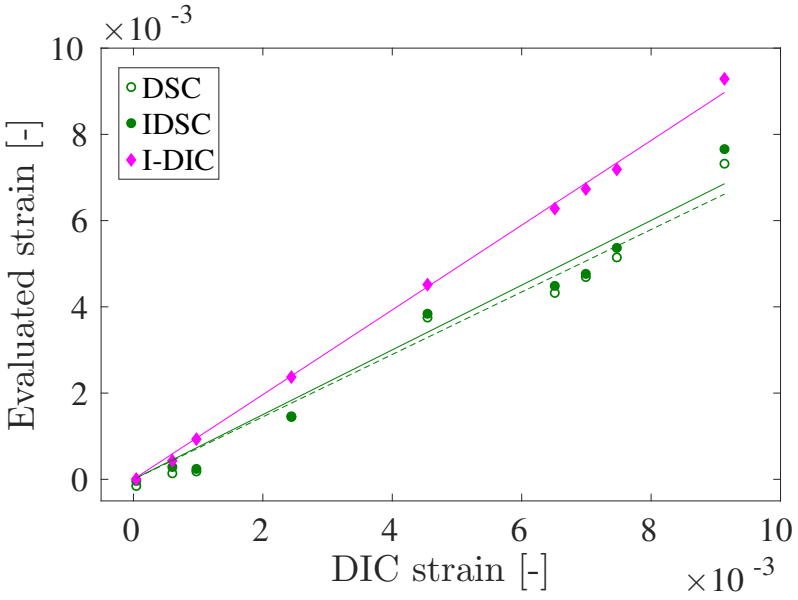

Fig. 24: Longitudinal elastic strains for the 10 loading steps with the four techniques

Unlike Ti64, there is a significant difference between both DIC estimates and the DSC results. This effect cannot be attributed to plasticity since linear relationships between DIC and integrated DIC results would not be observed. The explanation comes from the fact that DIC analyses are performed at the macroscale (*i.e.,* the two-phase alloy) whereas DSC analyses only consider the α-phase. In the present case, it is shown that the mean elastic strains evaluated in the α-phase are about 73 % those of the alloy (*i.e.,* at the macroscopic level). This difference is due to the presence of two phases in Ti5553 whose elastic properties are different [14,45,50,49,51,41]. Contrary to Ti64, which is mostly composed of α-phase, the presence of 40 $wt\%$ β-phase induces a deviation for the determination of macroscopic stresses using X-Ray elasticity constants of pure titanium. The deviation is estimated at 27 % in the present case.

Figure 25 shows the stress estimates for Ti5553. In the present case the DIC stresses (*i.e.,* the macroscopic stresses) are the reference. Independent tensile tests on the same alloy provided a Young's modulus of 115 GPa, and Poisson's ratio equal to 0.35. DIC and integrated DIC stresses

are close, which is consistent with the observations of Figure 24. The longitudinal stresses obtained with both DSC approaches are also in good agreement. By using the same elastic parameters for the α-phase as those considered for Ti64, the mean stress in the α-phase amounts to about 69 % of the macroscopic stress. This stress ratio is again due to the difference in elastic properties of α- and β-phases in this alloy [14, 45, 50, 49, 51, 41].

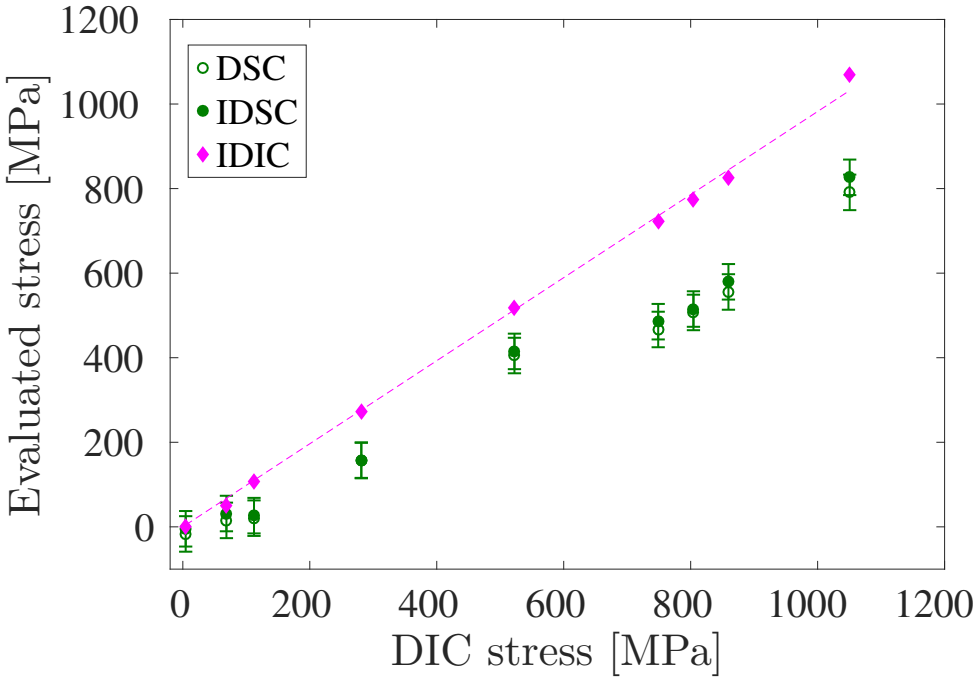

Fig. 25: Longitudinal stresses σ_ϕ in Ti5553 alloy evaluated via different techniques. The error bars depict the room mean square difference between DSC or IDSC estimates and the DIC stresses. The standard DIC stress uncertainty is equal to 30 MPa

The shear stresses are again very small (Figure 26). The mean level is 13.5 MPa for IDSC, and 15 MPa for DSC. Therefore, there is a small bias in the present case. It may be due to small misalignments of the goniometer (whose standard uncertainty was estimated to be 2°).

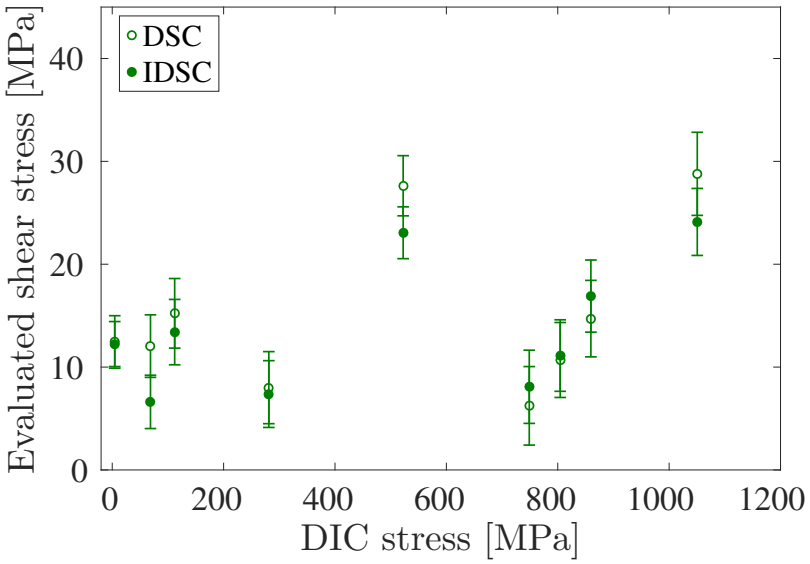

Fig. 26: Shear stress τ_ϕ in Ti5553 alloy coupon evaluated with DSC and IDSC. The error bars depict the room mean square difference between DSC or IDSC estimates and a vanishing shear stress. The standard DIC stress uncertainty is equal to 30 MPa

Figure 27 displays the standard stress resolution for XRD analyses and the the root mean square errors of DSC and IDSC results with respect to DIC stresses. The level of the standard resolution is 12 MPa for integrated DSC, and 13 MPa for DSC. A value 4 times higher than for Ti64 alloys is observed. This difference can be explained by the poor quality of diffraction peaks in Ti5553 alloys (Figure 5), which is expected for such alloys [18]. The root mean square errors for the stress estimations is respectively 45 MPa for DSC, and 49 MPa for IDSC (to be compared to 37 MPa, and 41 MPa for Ti64). Given the fact that the signal to noise ratio was significantly lower (*i.e.,* 4 times) for Ti5553 in comparison to Ti64, this 20 % increase of the stress uncertainty remains very modest.

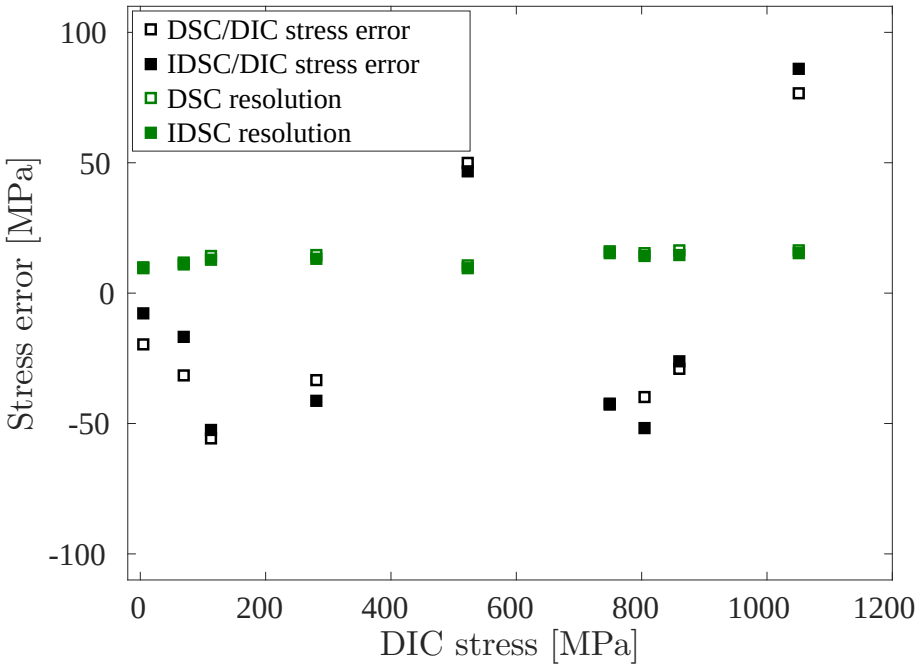

Fig. 27: Standard resolution and error of stress evaluations in Ti5553 alloy. The standard DIC stress uncertainty is equal to 30 MPa

The last step to validate the present results is to analyze the diffraction angle estimated for the α-phase of Ti5553. It is shown in Figure 28 that $2\theta_0 = 140.04°$ for IDSC and $2\theta_0 = 140.05°$ for DSC, which are close to the level obtained for Ti64 alloy (Figure 20). The small difference between both values can be explained by the changes in chemical composition and phase distributions. The corresponding standard deviations are equal to $0.0084°$ for IDSC, and 0.0088 for DSC. These levels lead to strain uncertainties of the order of 5.5×10^{-5}. The corresponding longitudinal stress uncertainties become ≈ 6 MPa. The present levels are even lower than those observed for Ti64 and do not contribute significantly to the overall uncertainties.

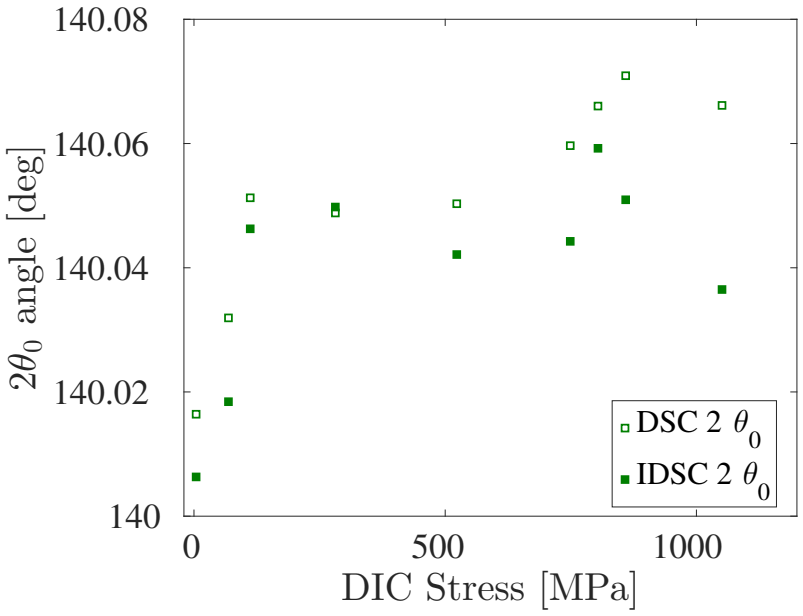

Fig. 28: Angle $2\theta_0$ for Ti5553 alloy. The standard DIC stress uncertainty is equal to 30 MPa

6 Conclusions

A validation procedure of stress evaluations via XRD has been proposed. It is based upon *in-situ* tensile tests. In the present case, the tensile stage was mounted within the goniometer. It is applied to two titanium alloys. The first one (Ti64) mostly contains an α-phase, which leads to well-formed diffraction peaks. Conversely, Ti5553 has a more complex microstructure that makes stress evaluations more challenging since the signal to noise ratio will be significantly lower than for Ti64. Having access to images acquired during the tests, digital image correlation (DIC) could also be utilized to evaluate strains and stresses.

Two registration techniques, in which the unstressed configuration does not need to be known, have been applied to XRD signals obtained for the two studied alloys. The first route consists in independently registering a known function (here a Gaussian) with the acquired diffractograms. From this information, the stress state is subsequently determined. The second route consists in

merging both steps into a single analysis. It is referred to as integrated diffraction signal correlation (*i.e.,* IDSC). It is shown that the latter leads to lower stress resolutions when compared to the former.

For Ti64 a very good agreement is observed between the stresses estimated with both DSC techniques, integrated DIC and regular DIC. For Ti5553, it is shown that the elastic strains in the α-phase are about 73 % of the macroscopic strain, which is due to the difference in elastic properties of the two phases. Further, the fact that the two DSC techniques yield virtually identical results validates the hypothesis of elasticity at the level of the α-phase. For both materials, it is observed that the diffraction angle for the unstressed state is very close to 140° (*i.e.,* the reference level for pure titanium).

Stress resolutions and uncertainties have been systematically analyzed for both alloys. In particular, it is shown that the uncertainty associated with the knowledge of the unstressed configuration has a limited impact on the overall levels. With the implemented registration techniques there is only a 20 % increase of overall stress uncertainties for Ti5553 with respect to Ti64 even though the peak height has been decreased by a factor of 4. This result validates the two registration techniques and shows their robustness even for Ti5553.

Having validated the present registration techniques, they can now be used in other configurations to study, for instance, the surface integrity [4–6] associated with different milling conditions of Ti5553 [2]. They may also be used in benchmarks with other materials and procedures [16, 17].

Acknowledgements This work was funded by Safran Landing Systems. The authors acknowledge Pierre Mella for providing Ti64 alloy and useful discussions on XRD analyses. The authors also thank Adam Cox for providing Ti5553 alloy samples and Thierry Bergey for electropolishing them.

References

1. M. Hill. Engineering residual stress in aerospace forgings. *Materials Research Proceedings*, 2:61–66, 2016.
2. A. Cox, J.-P. Villain-Chastre, S. Turner, and M. Jackson. The effect of finish milling on the surface integrity and surface microstructure in Ti-5Al-5Mo-5V-3Cr. 13th World Conference on Titanium, 2015.
3. E. Aeby-Gautier, A. Settefrati, F. Bruneseaux, B. Appolaire, B. Denand, M. Dehmas, G. Geandier, and P. Boulet. Isothermal α'' formation in β metastable titanium alloys. *Journal of Alloys and Compounds*, 577S:439–443, 2013.
4. G. Lütjering and J.C. Williams. *Titanium*. Springer, 2007.
5. N. Guillemot, C. Lartigue, R. Billardon, and B. Mawussi. Prediction of the endurance limit taking account of the microgeometry after finishing milling. *International Journal on Interactive Design and Manufacturing*, 4:239–249, 2010.
6. A. Souto-Lebel, N. Guillemot, C. Lartigue, and R. Billardon. Characterization and influence of defect size distribution induced by ball-end finishing milling on fatigue life. volume 19, pages 343–348. 1st CIRP Conference on Surface Integrity (CSI), 2011.
7. ASTM E837-13a, Standard test method for determining residual stresses by the hole-drilling strain-gage method. *ASTM International*, 2015.
8. M. Prime. Cross-sectional mapping of residual stresses by measuring the surface contour after a cut. *Journal of Engineering Materials and Technology*, 123 (2):162–168, 2001.
9. E. C. Reed Reed and J. A. Viens. The influence of surface residual stress on fatigue limit of titanium. *Journal of Engineering for Industry*, pages 82–76, 1960.
10. M.E. Fitzpatrick, A.T. Fry, P. Holdway, F.A. Kandil, J. Shackleton, and L. Suominen. Determination of residual stresses by x-ray diffraction - issue 2. *ISSN*, pages 1744–3911, 2005.
11. S. Freour, D. Gloaguen, M. François, R. Guillen, and E. Girard. Determination of the macroscopic elastic constants of a phase embedded in a multiphase polycrystal - application to the beta-phase of Ti17 titanium based alloy. *Materials Science Forum, Trans Tech Publications Inc.*, 404-407:723–728, 2002.
12. EN 15305, Non-destructive Testing, Test Method for Residual Stress analysis by X-ray Diffraction. *AFNOR*, 2009.
13. B. D. Cullity. Elements of x-ray diffraction. *American Journal of Physics*, 25:394, 1957.
14. V. Hauk. *Structural and Residual Stress Analysis by Non Destructive Methods: Evaluation, Application, Assessment*. Elsevier Science, Amsterdam, 1997.
15. W. Pfeiffer and E. Reisacher. Evaluation of thickness and residual stress of shallow surface regions from diffraction profiles. *Materials Research Proceedings*, (2):317–322, 2016.
16. F. Lefebvre, M. François, J. Cacot, C. Hemery, P. Le-Bec, E. Baumhauer, D. Bouscaud, T. Bergey, D. Blaize, D. Gloaguen, J. L. Lebrun, A. Cosson, R. Kubler, Y. Cheynet, E. Daniel, H. Michaud, J.C. Monvoisin, P. Blanchet, P. Allain, Y. Mrini, J. M. Sprauel, P. Goudeau, P. Barbarin, C. Charles, J.M. Le Roux, W. Seiler, C. Fischer, L. Desmas, A. Ouakka, M.J. Moya, and Y. Bordiec. External reference samples for residual stress analysis by x-ray diffraction. *Mat. Sci. Forum*, 681:215–222, 2011.

17. L. Suominen, T. Rickert, and S. Send. Residual Stress Measurement of Ti-Metal Samples by Means of XRD with Ti and Cu Radiation. *Materials Research Proceedings*, (2):61–66, 2016.
18. P.-J. Withers, M.-R. Daymondb, and M.W. Johnsonb. The precision of diffraction peak location. *J. Appl. Cryst.*, 34(Part 6):737–743, 2001.
19. Stressdiff. http://www.inel.fr.
20. Leptos by Bruker. https://www.bruker.com.
21. I.C. Noyan and J.B. Cohen. *Residual Stresses: Measurements by Diffraction and Interpretation*. Springer, New York, 1987.
22. G. Geandier, P.-O. Renault, E. Le Bourhis, Ph. Goudeau, D. Faurie, C. Le Bourlot, Ph. Djemia, O. Castelnau, and S. Cherif. Elastic strain distribution in metallic filmpolymer substrate composites. *Appl. Phys. Lett.*, 96, 2010.
23. G. Geandier, D. Thiaudière, R. N. Randriamazaoro, R. Chiron, S. Djaziri, B. Lamongie, Y. Diot, E. Le Bourhis, P. O. Renault, P. Goudeau, A. Bouaffad, O. Castelnau, D. Faurie, and F. Hild. Development of a synchrotron biaxial tensile device for in-situ characterization of thin films mechanical response. *Rev. Sci. Instrum.*, 81(103903), 2010.
24. M. Rekik, O. Hubert, L. Daniel, B. Raka, P. Mella, and P. Aimedieu. Dispositif de mesure du comportement magnéto-mécanique d'un alliage de fer-silicium sous chargement mécanique multiaxial. Congrès Français de Mécanique, 2013.
25. M.A. Sutton, J.J. Orteu, and H. Schreier. *Image correlation for shape, motion and deformation measurements: Basic Concepts, Theory and Applications*. Springer, New York, NY (USA), 2009.
26. S. Djaziri, P.O. Renault, F. Hild, E. Le Bourhis, P. Goudeau, D. Thiaudière, and D. Faurie. Combined synchrotron x-ray and image-correlation analyses of biaxially deformed w/cu nanocomposite thin films on kapton. *J. Appl. Cryst.*, 44:1071–1079, 2011.
27. S. Djaziri, D. Faurie, E. Le Bourhis, Ph. Goudeau, P.O. Renault, C. Mocuta, D. Thiaudière, and F. Hild. Investigation of the elastic-plastic transition of nanostructured thin film under controlled biaxial deformation. *Thin Solid Films*, 530:30–34, 2013.
28. F. Hild and S. Roux. Digital image correlation: From measurement to identification of elastic properties - a review. *Strain*, 42:69–80, 2006.
29. S. Roux and F. Hild. Stress intensity factor measurements from digital image correlation: post-processing and integrated approaches. *Int. J. Fract.*, 140(1-4):141–157, 2006.
30. H. Leclerc, J.N. Périé, S. Roux, and F. Hild. *Integrated digital image correlation for the identification of mechanical properties*, volume LNCS 5496, pages 161–171. Springer, Berlin (Germany), 2009.
31. J. Réthoré. A fully integrated noise robust strategy for the identification of constitutive laws from digital images. *Int. J. Num. Meth. Eng.*, 84(6):631–660, 2010.
32. J. Réthoré, Muhibullah, T. Elguedj, M. Coret, P. Chaudet, and A. Combescure. Robust identification of elasto-plastic constitutive law parameters from digital images using {3D} kinematics. *Int. J. Solids Struct.*, 50(1):73–85, 2013.

33. B. Beaubier, J.E. Dufour, F. Hild, S. Roux, S. Lavernhe-Taillard, and K. Lavernhe-Taillard. CAD-based calibration of a 3D-DIC system: Principle and application on test and industrial parts. *Exp. Mech.*, 54(3):329–341, 2014.
34. J.-E. Dufour, B. Beaubier, F. Hild, and S. Roux. CAD-based displacement measurements. Principle and first validations. *Exp. Mech.*, 55(9):1657–1668, 2015.
35. J.-E. Dufour, F. Hild, and S. Roux. Shape, Displacement and Mechanical Properties from Isogeometric Multiview Stereocorrelation. *J. Strain Analysis*, 50(7):470–487, 2015.
36. F. Hild, A. Bouterf, L. Chamoin, F. Mathieu, J. Neggers, F. Pled, Z. Tomičević, and S. Roux. Toward 4d mechanical correlation. *Adv. Mech. Simul. Eng. Sci.*, 3(1):1–26, 2016.
37. R. Boyer and R. Briggs. The use of beta titanium alloys in the aerospace industry. *J. Mater. Eng. Perform.*, 14:681–685, 2005.
38. E112-96, Standard Test Method for Determining Average Grain Size. *AFNOR*, pages 227–49, 1997.
39. J. Lu. Handbook of measurement of residual stresses. *Society for Experimental Mechanics*, 1996.
40. B. Voillot, F. Hild, J.L. Lebrun, and R. Billardon. Evaluation of residual stresses due to mechanical treatment of Ti5553 alloy via XRD. 13th World Conference on Titanium, 2015.
41. T. Duval, P. Villechaise, and S. Andrieu. Mechanical Properties and Strain Mechanisms Analysis in Ti5553 Titanium Alloy. *The Minerals, Metals & Materials Society (TMS)*, 2011.
42. B. Voillot, P. Aimedieu, P. Mella, J.L. Lebrun, and F. Hild. Evaluation des contraintes residuelles induites par traitements mecaniques dans un alliage de titane bi-phase par trois methodes de depouillement differentes. Congrès Mécamat, 2015.
43. M. Bertin, F. Hild, S. Roux, F. Mathieu, H. Leclerc, and P. Aimedieu. Integrated digital image correlation applied to elasto-plastic identification in a biaxial experiment. *J. Strain Anal.*, 51(2):118–131, 2016.
44. Christoph Leyens and Manfred Peters. *Titanium and titanium alloys: fundamentals and applications*. John Wiley & Sons, 2003.
45. S. Fréour, D. Gloaguen, M. François, and R. Guillen. Influence of a two-phase microstructure on XEC and XRD stress analysis. *Revue de Métallurgie*, 12:1185–1191, 2003.
46. G. Bruno and B.D. Dunn. Surface and Bulk Residual Stress in Ti6Al4V Welded Aerospace Tanks. *Pressure Vessel Technol*, 126(3):284–292, 2004.
47. F. Hild and S. Roux. *Digital Image Correlation*, pages 183–228. Wiley-VCH, Weinheim (Germany), 2012.
48. ISO/IEC guide 99-12:2007. *International Vocabulary of Metrology - Basic and General Concepts and Associated Terms, VIM*. International Organization for Standardization, Geneva (Switzerland), 2007.
49. G. Martin. *Simulation numerique multi-echelles du comportement mecanique des alliages de titane beta-metastable Ti5553 et Ti17*. PhD thesis, Ecole Nationale Superieure des Mines de Paris, 2012.
50. Sylvain Fréour, Emmanuel Lacoste, Manuel François, and Ronald Guillén. Determining ti-17 β-phase single-crystal elasticity constants through x-ray diffraction and inverse scale transition model. In *Materials Science Forum*, volume 681, pages 97–102. Trans Tech Publ, 2011.
51. M. Herbig. *D short fatigue crack investigation in beta titanium alloys using phase and diffraction contrast tomography*. PhD thesis, INSA Lyon, 2011.